Optimization of Active and Reactive Power Dispatch among Multi-Paralleled Grid-Connected Inverters Considering Low-Frequency Stability

Zhou, Weihua; Wang, Yanbo; Liu, Dong; Chen, Zhe

Published in:
Proceedings of IECON 2019 - 45th Annual Conference of the IEEE Industrial Electronics Society

DOI (link to publication from Publisher):
10.1109/IECON.2019.8927560

Publication date:
2019

Document Version
Accepted author manuscript, peer reviewed version

Optimization of Active and Reactive Power Dispatch among Multi-Paralleled Grid-Connected Inverters Considering Low-Frequency Stability

Weihua Zhou*, Yanbo Wang†, Dong Liu‡,and Zhe Chen§
Department of Energy Technology
Aalborg University
Aalborg, Denmark
*wez@et.aau.dk, †ywa@et.aau.dk, ‡dli@et.aau.dk, §zch@et.aau.dk

***Abstract*—This paper presents an optimization method of active and reactive power dispatch among multi-paralleled voltage source grid-connected inverters (GCIs) considering stability enhancement in low-frequency range. DQ impedance model of GCI with outer power control loop, inner current control loop and phase-locked loop (PLL) is first established. Then, influences of active and reactive power references on terminal impedance frequency characteristics of GCI, e.g., passivity, are theoretically derived. It's found that more active power tends to destabilize the power system, and more reactive power tends to stabilize the power system. On the basis of it, an active and reactive power dispatch method for stability enhancement in low-frequency range is proposed, where more/less active power and less/more reactive power are allocated to the GCIs with narrow/wide bandwidths of power control loop and PLL. Simulation of a five-GCIs-based power system is performed to validate the proposed active and reactive power dispatch method considering low-frequency stability enhancement.**

***Index Terms*—Active power, DQ impedance model, grid-connected inverter, low-frequency stability, optimization, reactive power.**

I. Introduction

Renewable energies, such as wind power and solar power, have been increasingly exploited in recent years. Voltage source grid-connected inverters (GCIs) are commonly used to transmit the generated electricity to utility grid [1]. However, impedance interaction between control loops of GCIs and grid sometimes leads to instability phenomena, thus influencing system safe and reliable operation [2]–[7].

Instability mechanism and corresponding resonance mitigation methods for single GCI have been widely developed in recent years [4], [8]–[12]. Harmonic resonance induced by interaction between current control loop and grid impedance is related with only LCL filter, current controller parameters and sampling frequency, which is independent on operation point [5], [7]. However, when further considering power control loop and phase-locked loop (PLL), system stability is dependent on operation points, e.g., active and reactive power/current references, due to nonlinear characteristics of power control loop and PLL [4], [9]–[12]. In detail, as for active power, high active power level tends to weaken the stability of VSC-HVDC system [9]. Furthermore, stability of the VSC-HVDC system can be altered if flow direction of active power is changed [10]. As for reactive power, it's found that flow direction of reactive power, i.e, the inductive or capacitive reactive power, can impact dq-channel component of DQ impedance model of GCI under dc-link voltage control, and further has reverse impacts on the stability of the dc-link voltage control under a weak grid condition [11]. Furthermore, impact of inductive reactive power level on the stability of offshore wind power plant in low-frequency range has been analyzed recently. However, whether active and reactive power can be employed to mitigate resonance phenomena of single GCI has not been investigated yet [9]–[11].

On the other hand, stability analysis and resonance damping of multi-paralleled GCIs have been reported in [2], [3], [13]–[15]. Circuit and controller parameters of paralleled GCIs are assumed as the same in [2], [3], [13]. Furthermore, stability analysis of multi-paralleled GCIs with different LCL filters and sampling frequencies is performed in [14]. Conventionally, controller parameters are re-tuned when resonance phenomena occur [16], [17]. However, system dynamic performance may be weakened. In [15], passivity of multi-paralleled GCIs is enhanced by carefully designing LCL filter parameters, sampling frequencies and control strategies, i.e., grid-side current control and inverter-side current control, so that the non-passivity regions of GCIs can be canceled. Therefore, the system can be stabilized without controller re-tuning and active damping. However, only high-frequency instability phenomena caused by current control loop instead of power control loop and PLL are investigated. In addition, only circuit and controller parameters of paralleled GCIs instead of operation points are optimized in [15]. In practice, GCIs are sometimes controlled to inject a certain amount of reactive power. Reactive power dispatch among paralleled GCIs is sometimes optimized to improve power transfer capability under ultra-weak grid con-

This work was supported by the ForskEL and EUDP project "Voltage Control and Protection for a Grid towards 100% Power Electronics and Cable Network (COPE)" (Project No.: 880063).

ditions [18], to better control the voltages and faster recover the violated voltage when compared with only using reactive power compensation devices [19], [20]. However, from the perspective of stability, whether re-distribution of active and reactive power influences system stability has not been investigated yet.

To fill the research gap, this paper presents an optimization method of active and reactive power dispatch among multi-paralleled GCIs with different circuit and controller parameters considering low-frequency stability. The main contributions of the paper are summarized as follows. (1) Impacts of active and reactive power on passivity of GCI in low-frequency range are theoretically derived. (2) Dispatch of active and reactive power among multi-paralleled GCIs is optimized to mitigate low-frequency instability phenomena.

The rest of this paper is organized as follows. In Section II, system configuration of the studied multi-paralleled GCI system and impedance model are introduced, based on which impacts of active and reactive power on system passivity are theoretically derived. Case studies are given in Section III to valid the correctness of the findings in Section II. In Section IV, time-domain simulation verification is performed. Finally, conclusions are drawn in Section V.

II. System Modelling and Power Characteristics Analysis

In this section, configuration of the studied power system is first depicted, followed by the introduction of impedance modelling of GCI in dq reference frame with consideration of power control loop, current control loop and PLL. On the basis of it, impacts of active and reactive power references on passivity of GCI are theoretically derived.

A. System Modelling

Fig. 1 shows circuit configuration of an exemplified power system which consists of five L-filtered GCIs connected with point of common coupling (PCC) in parallel. DC-link voltage of each GCI V_{dc} is regarded as constant. In addition, each GCI is under PQ-controlled. The detailed control system are omitted here, which can be found in [4]. Grid impedance Z_g is modelled as a parasitic capacitor C_g in parallel with a resistor R_g and an inductor L_g.

Fig. 2 shows control block diagram of GCI 1 in Fig. 1, based on which dq impedance model of the GCI can be derived as (1), where the detailed expressions of all elements in (1) can be found in [4]. To clearly observe impacts of parameters on $\mathbf{Z_{dq}(s)}$, detailed expressions of all elements are substituted into (1), and $\mathbf{Z_{dq}(s)}$ is re-formulated as (2), where terms A, B, C, D, E and F are expressed as the second parts of equations in (3).

After obtaining the dq impedance model of single GCI, total impedance of the five paralleled GCIs $\mathbf{Z_{tot}}$ can be calculated based on basic circuit principle. Similarly, grid impedance in dq reference frame $\mathbf{Z_g}$ can be calculated, shown as follows,

$$\begin{aligned}\mathbf{Z_{tot}} &= \mathbf{Z_{GCI1}}//\mathbf{Z_{GCI2}}//\mathbf{Z_{GCI3}}//\mathbf{Z_{GCI4}}//\mathbf{Z_{GCI5}}\\ \mathbf{Z_g} &= (\mathbf{Z_{L_g}} + \mathbf{Z_{R_g}})//\mathbf{Z_{C_g}}\end{aligned} \tag{4}$$

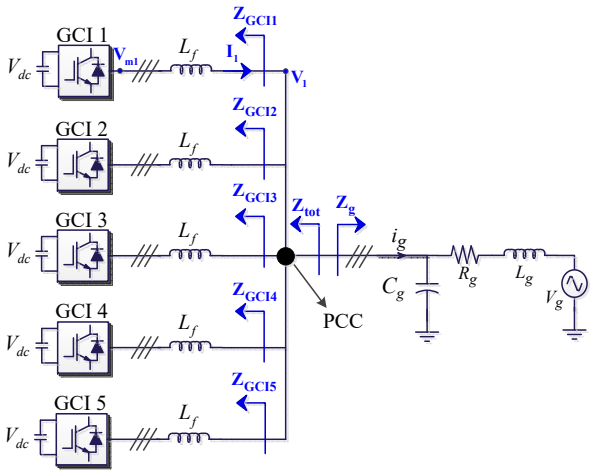

Fig. 1. Typical circuit configuration of a multi-paralleled GCI system.

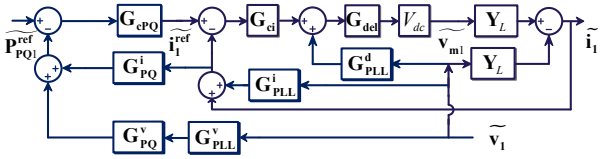

Fig. 2. Control block diagram of GCI 1 with outer power control, inner current control loop and PLL.

Impedance model of the whole power system is shown in Fig. 3. System stability can then be assessed by checking whether Nyquist plots of eigenvalues of $\mathbf{T_m} = \mathbf{Z_g Z_{tot}^{-1}}$ encircle critical point $(-1, j0)$ in complex plane or not [4].

B. Impacts of Active and Reactive Power References on Passivity of GCI

1) Reformulation of dq Impedance Model: Take GCI 1 as an example. When the power system reaches steady state, power reference $\mathbf{P_{PQ1}^{ref}} = P_{ref} + jQ_{ref}$ of GCI 1 can be calculated as follows,

$$\begin{aligned}P_{ref} &= V_d I_d + V_q I_q\\ Q_{ref} &= V_d I_q - V_q I_d\end{aligned} \tag{5}$$

where $\mathbf{V_1} = V_d + jV_q$ and $\mathbf{I_1} = I_d + jI_q$ are terminal voltage and current vectors, respectively. Since d axis of the dq reference frame is aligned with $\mathbf{V_1}$, $V_d = \mathbf{V_1} = |\mathbf{V_1}| = V_1$, $V_q = 0$. Steady-state I_d and I_q can then be calculated as follows,

$$\begin{aligned}I_d &= \frac{P_{ref}}{V_1}\\ I_q &= \frac{Q_{ref}}{V_1}\end{aligned} \tag{6}$$

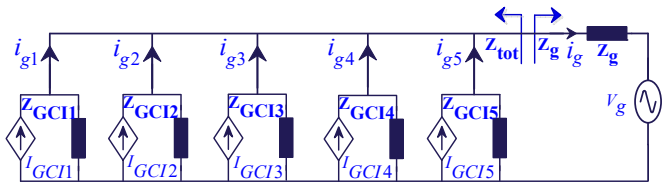

Fig. 3. Impedance model of the multi-paralleled GCI system in Fig. 1.

$$\begin{aligned}\mathbf{Z_{dq}}(s) =&\mathbf{V_1}\mathbf{I_1^{-1}} = (\mathbf{Z_{out}^{-1}}(s) + \mathbf{G_{id}}(s)\mathbf{G_{del}}(s)(\mathbf{G_{PLL}^{d}}(s) - \mathbf{G_{ci}}(s)\mathbf{G_{cPQ}}(s)\mathbf{G_{PQ}^{v}}(s)\mathbf{G_{PLL}^{v}}(s) - (\mathbf{G_{ci}}(s)\mathbf{G_{cPQ}}(s)\mathbf{G_{PQ}^{i}}(s)\\ &+ \mathbf{G_{ci}}(s) + \mathbf{G_{dei}}(s))\mathbf{G_{PLL}^{i}}(s))K)^{-1}(\mathbf{I} + \mathbf{G_{id}}(s)\mathbf{G_{del}}(s)(\mathbf{G_{ci}}(s)\mathbf{G_{cPQ}}(s)\mathbf{G_{PQ}^{i}}(s) + \mathbf{G_{ci}}(s) - \mathbf{G_{dei}}(s))K)\end{aligned} \tag{1}$$

$$\mathbf{Z_{dq}(s)} = \begin{bmatrix} Z_{dd}(s) & Z_{dq}(s) \\ Z_{qd}(s) & Z_{qq}(s) \end{bmatrix} = \begin{bmatrix} \frac{CE}{A} + \frac{BD}{A} & \frac{BE}{A} - \frac{CD}{A} \\ \frac{H_{PQ}H_{cc}H_{pwm}I_qB}{A} - \frac{CF}{A} & -\frac{BF}{A} - \frac{H_{PQ}H_{cc}H_{pwm}I_qC}{A} \end{bmatrix} \tag{2}$$

$$\begin{aligned}A =& H_{PQ}^2H_{cc}^2H_{pwm}^2(I_d^2 + I_q^2) + T_{PLL}H_{PQ}H_{cc}^2H_{pwm}^2(I_d^2 + I_q^2) + T_{PLL}H_{PQ}H_{cc}H_{pwm}^2(D_dI_d + D_qI_q) + T_{PLL}H_{pwm}\cdots\\ &(H_{cc}I_d + K_dI_q + D_d) - 1 = H_{PQ}H_{cc}^2H_{pwm}^2(H_{PQ} + T_{PLL})\frac{(P_{ref}^2 + Q_{ref}^2)}{V_1^2} + \frac{T_{PLL}H_{PQ}H_{cc}H_{pwm}^2}{0.5V_{dc}}P_{ref} + T_{PLL}H_{pwm}\cdots\\ &(\frac{H_{cc}P_{ref}}{V_1} + \frac{V_1}{0.5V_{dc}} + (K_d - \frac{\omega_1L_{f1}}{0.5V_{dc}})\frac{Q_{ref}}{V_1}) - 1\\ B =& R_{f1} + L_{f1}s + \frac{H_{pwm}V_{dc}\,(H_{cc} + H_{PQ}H_{cc}V_d)}{2} = R_{f1} + L_{f1}s + \frac{H_{pwm}V_{dc}\,(H_{cc} + H_{PQ}H_{cc}V_1)}{2}\\ \mathrm{C} =& L_{f1}\omega_1 - \frac{H_{pwm}V_{dc}(K_d + H_{cc}H_{PQ}V_q)}{2} = L_{f1}\omega_1 - \frac{H_{pwm}V_{dc}K_d}{2}\\ \mathrm{D} =& \mathrm{D}_dH_{pwm}T_{PLL} + H_{cc}H_{PQ}H_{pwm}I_d + H_{cc}H_{pwm}I_dT_{PLL} + H_{pwm}I_qK_dT_{PLL} - 1\\ =& \frac{V_1}{0.5V_{dc}}H_{pwm}T_{PLL} - 1 + H_{cc}H_{pwm}(H_{PQ} + T_{PLL})\frac{P_{ref}}{V_1} + H_{pwm}T_{PLL}(K_d + \frac{-\omega_1L_{f1}}{0.5V_{dc}})\frac{Q_{ref}}{V_1}\\ E =& \mathrm{D}_qH_{pwm}T_{PLL} + H_{cc}H_{PQ}H_{pwm}I_q + H_{cc}H_{pwm}I_qT_{PLL} - H_{pwm}I_dK_dT_{PLL}\\ =& (\frac{\omega_1L_{f1}}{0.5V_{dc}} - K_d)H_{pwm}T_{PLL}\frac{P_{ref}}{V_1} + H_{cc}H_{pwm}(H_{PQ} + T_{PLL})\frac{Q_{ref}}{V_1}\\ F =& 1 + H_{cc}H_{PQ}H_{pwm}I_d = 1 + H_{cc}H_{PQ}H_{pwm}\frac{P_{ref}}{V_1}\end{aligned} \tag{3}$$

Based on $\mathbf{V_1}$ and $\mathbf{I_1}$, output voltage $\mathbf{V_{m1}}$ of GCI 1 can be obtained by applying the Ohm's law on the filter inductor L_f, shown as follows,

$$\mathbf{V_{m1}} = 0.5V_{dc}\mathbf{D_1} = \mathbf{V_1} + j\omega_1L_f\mathbf{I_1} \tag{7}$$

where $\mathbf{D_1} = D_d + jD_q$ is the duty cycle vector. Therefore, D_d and D_q can be obtained as follows,

$$\begin{aligned}D_d &= \frac{V_1 - \omega_1L_{f1}I_q}{0.5V_{dc}} = \frac{V_1 - \omega_1L_{f1}\frac{Q_{ref}}{V_1}}{0.5V_{dc}}\\ D_q &= \frac{\omega_1L_{f1}I_d}{0.5V_{dc}} = \frac{\omega_1L_{f1}\frac{P_{ref}}{V_1}}{0.5V_{dc}}\end{aligned} \tag{8}$$

By substituting (6) and (8) into (3), terms A, B, C, D, E and F can be represented by controller parameters of power control loop, current control loop and PLL, P_{ref}, Q_{ref} and V_1, shown as the third parts of all equations in (3). On the basis of it, influences of P_{ref} and Q_{ref} on passivity of GCI can be theoretically analyzed.

2) Impacts of Active and Reactive Power References on Passivity of GCI: Since component Z_{qq} plays an important role in stability assessment, investigation of impacts of P_{ref} and Q_{ref} on Z_{qq} is focused. Z_{qq} in (2) is reformulated as follows,

$$Z_{qq}(s) = \frac{-BF - H_{PQ}H_{cc}H_{pwm}I_qC}{A} = \frac{\Gamma_1 + \Gamma_2P_{ref} + \Gamma_3Q_{ref}}{A} \tag{9}$$

where Γ_1, Γ_2 and Γ_3 are shown as follows,

$$\begin{aligned}\Gamma_1 &= \frac{H_{pwm}V_{dc}(H_{cc} + H_{PQ}H_{cc}V_1)}{2}\\ \Gamma_2 &= -\frac{H_{cc}H_{PQ}H_{pwm}(2R_{f1} + V_{dc}H_{pwm}(H_{cc} + H_{PQ}H_{cc}V_1))}{2V_1}\\ &\quad -\frac{H_{cc}H_{PQ}H_{pwm}L_{f1}s}{V_1} = -\Gamma_{2\_1} - \Gamma_{2\_2}s\\ \Gamma_3 &= \frac{H_{cc}H_{PQ}H_{pwm}(2L_{f1}\omega_1 - H_{pwm}V_{dc}K_d)}{2V_1}\end{aligned} \tag{10}$$

To simplify the analysis process of $\angle Z_{qq}$, PLL dynamics is neglected, i.e., $T_{PLL} = 0$. In addition, H_{PQ}, H_{cc} and H_{pwm} are regarded as constant for simplicity. Decoupling term K_d is regarded as 0. Term A in (3) can be simplified as follows,

$$A \approx A' = \frac{H_{PQ}^2H_{cc}^2H_{pwm}^2(P_{ref}^2 + Q_{ref}^2)}{V_1^2} - 1 \tag{11}$$

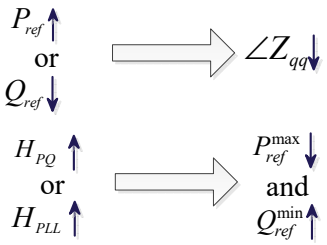

Fig. 4. Impacts of P_{ref} and Q_{ref} on $\angle Z_{qq}$ and impacts of H_{PQ} and H_{PLL} on P_{ref}^{max} and Q_{ref}^{min}.

Then, $\angle Z_{qq}$ at a specific frequency point ω_0 can be derived as follows,

$$\angle Z_{qq}|_{s=j\omega_0} = \arctan \frac{-\Gamma_{2\_2} P_{ref} \omega_0}{\Gamma_1 - \Gamma_{2\_1} P_{ref} + \Gamma_3 Q_{ref}} \tag{12}$$

Note that all the elements in (12) are positive. If $\angle Z_{qq}$ is required to be within $[-90^o, 90^o]$, real part of Z_{qq} should satisfy the following constraint.

$$real(Z_{qq}) = \Gamma_1 - \Gamma_{2\_1} P_{ref} + \Gamma_3 Q_{ref} \geq 0 \tag{13}$$

(13) indicates that low P_{ref} and high Q_{ref} tend to enforce the passivity of Z_{qq}. In detail, for a given Q_{ref}, passivity of Z_{qq} can be enforced if,

$$P_{ref} \leq P_{ref}^{\max} = \frac{\Gamma_1 + \Gamma_3 Q_{ref}}{\Gamma_{2\_1}} = P_{ref}^{\max 1} + P_{ref}^{\max 2} \tag{14}$$

On the other hand, for a given P_{ref}, passivity of Z_{qq} can be enforced if,

$$Q_{ref} \geq Q_{ref}^{\min} = \frac{\Gamma_{2\_1} P_{ref} - \Gamma_1}{\Gamma_3} = Q_{ref}^{\min 1} + Q_{ref}^{\min 2} \tag{15}$$

where $P_{ref}^{\max 1}$ and $Q_{ref}^{\min 1}$ are defined as follows,

$$\begin{aligned} P_{ref}^{\max 1} &= \frac{\Gamma_1}{\Gamma_{2\_1}} = \frac{V_1}{H_{cc} H_{PQ} H_{pwm}} \\ Q_{ref}^{\min 1} &= \frac{-\Gamma_1}{\Gamma_3} = -\frac{V_1 V_{dc}}{2 L_{f1} \omega_1} \left(\frac{1}{H_{PQ} + V_1}\right) \end{aligned} \tag{16}$$

It can also be seen from (14)-(16) that $P_{ref}^{\max}$ and $Q_{ref}^{\min}$ are sensitive to PQ controller parameters H_{PQ}. In detail, large H_{PQ} leads to small $P_{ref}^{\max}$ and larger $Q_{ref}^{\min}$. The conclusions are the same when it comes to PLL controller parameters T_{PLL}. The derivation process is omitted for simplicity. The findings are summarized in Fig. 4.

C. Flowchart of the Proposed Optimization Method of Active and Reactive Power Dispatch

Flowchart of the proposed optimization method of active and reactive power dispatch is shown in Fig. 5, which consists of three steps. In step 1, grid impedance, circuit and controller parameters of all GCIs, desired total active and reactive power P_{tot} and Q_{tot}, constraints of active and reactive power references of the N paralleled GCIs P_{k_limi} and Q_{k_limi} $(k = 1, 2..., N)$ are inputted. In step 2, active and reactive power references of the kth GCI P_{k_ref} and Q_{k_ref} are randomly set with constraint of P_{k_limi} and Q_{k_limi}

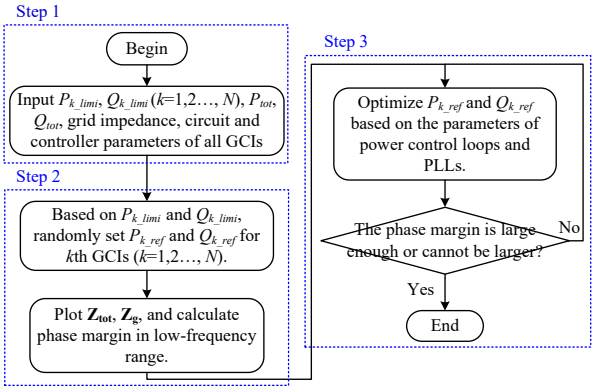

Fig. 5. Flowchart of the proposed optimization method of active and reactive power dispatch among multi-paralleled GCI system considering low-frequency stability.

$(k = 1, 2..., N)$. Then, phase margin in low-frequency range is obtained from Bode diagrams of $\mathbf{Z_{tot}}$ and $\mathbf{Z_g}$. In step 3, P_{k_ref} and Q_{k_ref} are simultaneously optimized based on the parameters of power control loops and PLLs. In detail, The GCIs with large bandwidths of power control loops and PLLs should have small P_{ref} and large Q_{ref}. If the re-designed phase margin is large enough or cannot be larger by optimizing active and reactive power distribution, the optimization process is completed. Otherwise, active and reactive power are re-distributed among the N paralleled GCIs, until phase margin is large enough or cannot be larger anymore.

III. Case Demonstration of Impacts of Active and Reactive Power on GCI Passivity

In this section, correctness of active and reactive power characteristics and their influences on GCI passivity is verified by Matlab/Simulink.

A. Impacts of Active and Reactive Power on GCI Passivity

Table I shows the parameters of LCL filters and current controllers of the five GCIs in Fig. 1. In addition, controller parameters of power control loop and PLL of GCI 1 are $k_{pPQ} = 2.7454e-5$, $k_{iPQ} = 0.01648$, $k_{ppll} = 20$ and $k_{ipll} = 200$. Fig. 6(a) shows Bode diagrams of GCI 1 impedance matrices obtained by frequency sweeping, where $Q_{ref} = 0$ MVar and P_{ref} is 0.1 MW, 0.5 MW, 1.0 MW, 1.5 MW and 2.0 MW, respectively. To more clearly observe the relationship between $\angle Z_{qq}$ and P_{ref}, $\angle Z_{qq}$ is zoomed in Fig. 6(b), and change curves of $\angle Z_{qq}$ with P_{ref} at 26 Hz, 31 Hz, 34 Hz, 37 Hz and 40 Hz are plotted in Fig. 6(c). It can be seen that $\angle Z_{qq}$ is decreased continuously as P_{ref} is increased. In addition, Z_{qq} becomes non-passive once P_{ref} exceeds a certain threshold value, and Z_{qq} is more likely to become non-passive in low-frequency range. The frequency sweeping results agree with the theoretical analysis results in Section II(B).

In addition, by changing the PLL parameters of GCI 1 from $k_{pll} = 20$, $k_{ipll} = 200$ to $k_{pll} = 2$, $k_{ipll} = 2$, Bode diagrams of GCI 1 impedance matrices are plotted in Fig. 7(a). $\angle Z_{qq}$

TABLE I
CIRCUIT AND CURRENT CONTROLLER PARAMETERS OF THE FIVE GCIS IN FIG. 1

Parameter	V_{dc}	L_{f1}	L_{f2}	C_f	k_{pi}	k_{ii}
Values	1150 V	263 μH	200 μH	40 μF	5.4908e-4	0.3295

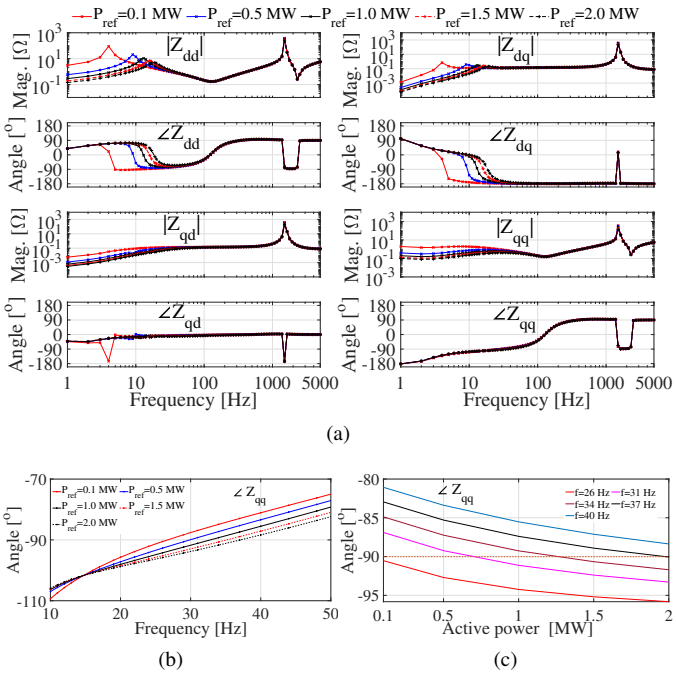

Fig. 6. Case 1 of GCI 1 with $k_{pPQ} = 2.7454e-5$, $k_{iPQ} = 0.01648$, $k_{ppll} = 20$, $k_{ipll} = 200$, $Q_{ref} = 0$ and different P_{ref}. (a) Bode diagrams of measured $\mathbf{Z_{dq}}$. (b) Zoomed $\angle Z_{qq}$. (c) Variation of $\angle Z_{qq}$ with P_{ref}.

is zoomed in Fig. 7(b), and change curves of Z_{qq} with P_{ref} at 26 Hz, 31 Hz, 34 Hz, 37 Hz and 40 Hz are plotted in Fig. 7(c). By comparing Figs. 6(c) and 7(c), it can be seen that the maximum active power reference $P_{ref}^{\max}$ not to violate the passivity of Z_{qq} increases as PLL bandwidth decreases. The frequency sweeping results agree with the theoretical analysis results in Section II(B).

Next, Fig. 8(a) shows Bode diagrams of GCI 1 impedance matrices when $P_{ref} = 2$ MW and Q_{ref} is 0.1 MVar, 0.5 MVar, 1.0 MVar, 1.5 MVar and 2.0 MVar, respectively. $\angle Z_{qq}$ is zoomed in Fig. 8(b), and Fig. 8(c) shows change curves of $\angle Z_{qq}$ with Q_{ref} at 12 Hz, 14 Hz, 17 Hz, 20 Hz and 26 Hz. It can be seen that $\angle Z_{qq}$ is increased continuously as Q_{ref} is increased. In addition, Z_{qq} becomes passive once Q_{ref} exceeds a certain threshold value. The frequency sweeping results agree with the theoretical analysis results in Section II(B).

B. Impact of Power Control Loop Parameters on $P_{ref}^{\max}$ and $Q_{ref}^{\min}$

By changing controller parameters of power control loop from $k_{pPQ} = 2.7454e-5$, $k_{iPQ} = 0.01648$ of case 2 to $k_{pPQ} = 5.4908e-5$, $k_{iPQ} = 0.03295$ of case 4, Fig. 9(a) shows Bode diagrams of GCI 1 impedance matrices when

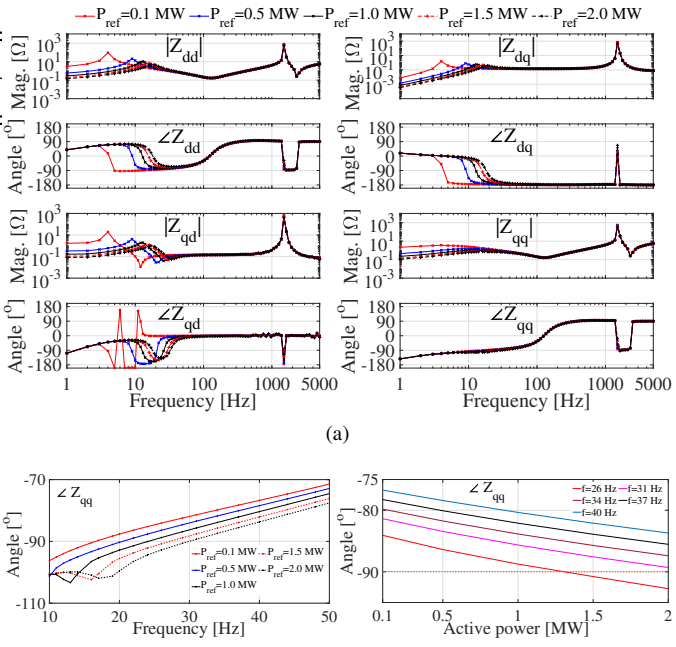

Fig. 7. Case 2 of GCI 1 with $k_{pPQ} = 2.7454e-5$, $k_{iPQ} = 0.01648$, $k_{ppll} = 2$, $k_{ipll} = 2$, $Q_{ref} = 0$ and different P_{ref}. (a) Bode diagrams of measured $\mathbf{Z_{dq}}$. (b) Zoomed $\angle Z_{qq}$. (c) Variation of $\angle Z_{qq}$ with P_{ref}.

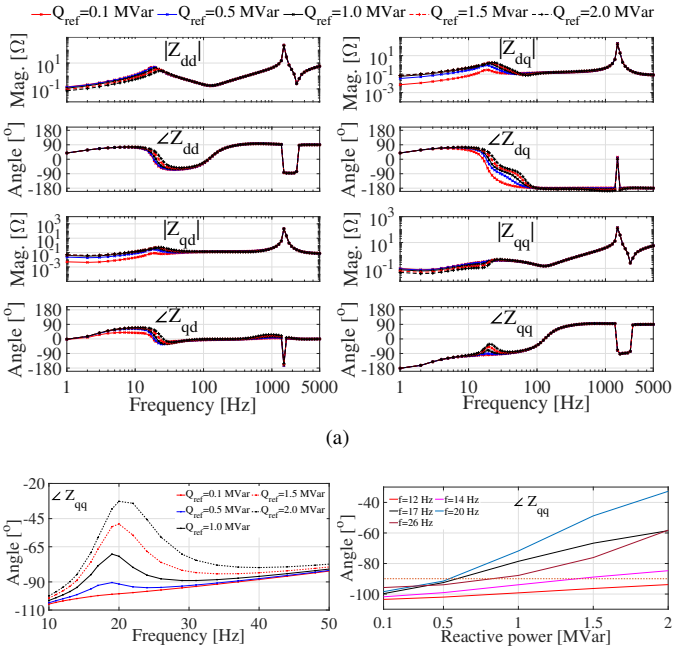

Fig. 8. Case 3 of GCI 1 with $k_{pPQ} = 2.7454e-5$, $k_{iPQ} = 0.01648$, $k_{ppll} = 20$, $k_{ipll} = 200$, $P_{ref} = 2$ MW and different Q_{ref}. (a) Bode diagrams of measured $\mathbf{Z_{dq}}$. (b) Zoomed $\angle Z_{qq}$. (c) Variation of $\angle Z_{qq}$ with Q_{ref}.

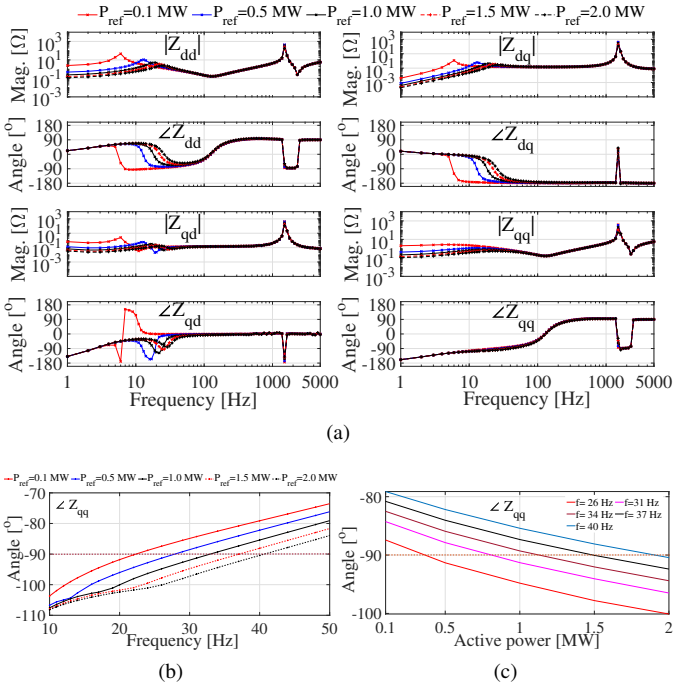

(a)

(b) (c)

Fig. 9. Case 4 of GCI 1 with $k_{pPQ} = 5.4908e-5$, $k_{iPQ} = 0.03295$, $k_{ppll} = 2$, $k_{ipll} = 2$, $Q_{ref} = 0$ and different P_{ref}. (a) Bode diagrams of measured $\mathbf{Z_{dq}}$. (b) Zoomed $\angle Z_{qq}$. (c) Variation of $\angle Z_{qq}$ with P_{ref}.

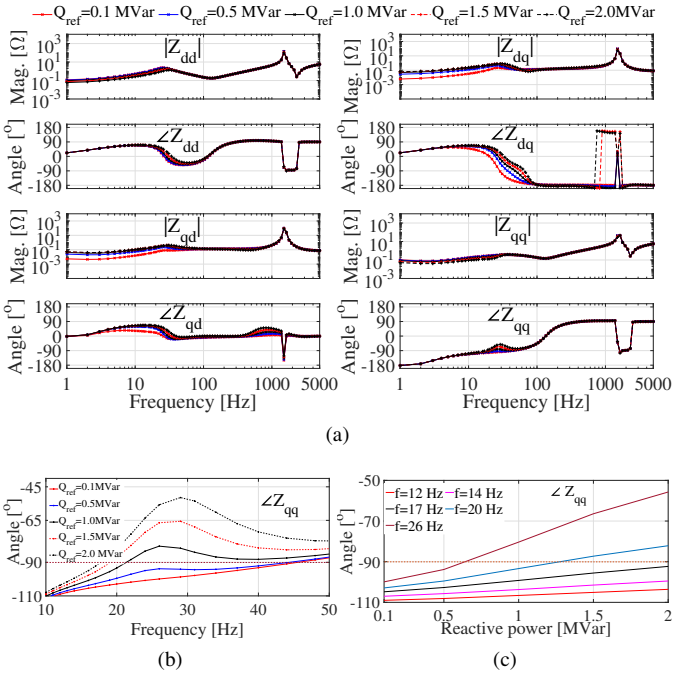

(a)

(b) (c)

Fig. 10. Case 5 of GCI 1 with $k_{pPQ} = 5.4908e-5$, $k_{iPQ} = 0.03295$, $k_{ppll} = 20$, $k_{ipll} = 200$, $P_{ref} = 2$ MW and different Q_{ref}. (a) Bode diagrams of measured $\mathbf{Z_{dq}}$. (b) Zoomed $\angle Z_{qq}$. (c) Variation of $\angle Z_{qq}$ with Q_{ref}.

$Q_{ref} = 0$ MVar and P_{ref} is 0.1 MW, 0.5 MW, 1.0 MW, 1.5 MW and 2.0 MW, respectively. $\angle Z_{qq}$ is zoomed in Fig. 9(b), and change curves of $\angle Z_{qq}$ with P_{ref} at 26 Hz, 31 Hz, 34 Hz, 37 Hz and 40 Hz are plotted in Fig. 9(c). It can be seen from Figs. 7(c) and 9(c) that maximum active power reference $P_{ref}^{\max}$ not to violate the passivity of Z_{qq} decreases as H_{PQ} increases, which agrees with the theoretical analysis results in Section II(B).

In addition, by changing the PLL parameters from $k_{pll} = 2$, $k_{ipll} = 2$ of case 4 to $k_{pll} = 20$, $k_{ipll} = 200$ of case 5, Fig. 10(a) shows Bode diagrams of GCI 1 impedance matrices when $P_{ref} = 2$ MW and Q_{ref} is 0.1 MVar, 0.5 MVar, 1.0 MVar, 1.5 MVar and 2.0 MVar, respectively. $\angle Z_{qq}$ is zoomed in Fig. 10(b), and change curves of $\angle Z_{qq}$ with Q_{ref} at 12 Hz, 14 Hz, 17 Hz, 20 Hz and 26 Hz are plotted in Fig. 10(c). By comparing Figs. 8(c) and 10(c), it can be seen that minimum reactive power reference $Q_{ref}^{\min}$ to enforce the passivity of Z_{qq} increases as H_{PQ} increases, which agrees with the theoretical analysis results in Section II(B).

IV. Time-domain Simulation Verification

Besides the circuit and current controller parameters of the five GCIs shown in Table 1, controller parameters of the PLLs of the five GCIs are assumed as the same $k_{ppll} = 20$ and $k_{ipll} = 200$. The only differences of the five GCIs are controller parameters of power control loops, as shown in Table II, where GCI 1 has the smallest power control loop bandwidth, and GCI 5 has the largest power control loop bandwidth.

Assume that the desired total active power P_{tot} and total reactive power Q_{tot} are 5 MW and 2.5 MVar, respectively. Table III shows four schemes of active and reactive power dispatch among the paralleled five GCIs. P_{tot} and Q_{tot} are evenly dispatched among the five GCIs in scheme 1. Bode diagrams of total dq impedance matrices of the five GCIs $\mathbf{Z_{s1}}$ and grid $\mathbf{Z_g}$ are plotted in Fig. 11(a). Bode diagrams of Z_{qq} are zoomed in Fig. 11(b). It can be seen that $\angle Z_{qq}$ at magnitude interaction point 32 Hz is lower than -90^o, and phase angle difference is thus larger than 180^o, which indicates that the system is unstable. Time-domain simulation results in Fig. 12 validate the correctness of the theoretical analysis result. On the other hand, if scheme 2 is adopted, i.e., lower active power and higher reactive power are allocated to the GCIs with larger power control loop parameters, Bode diagrams of total dq impedance matrix of the five GCIs $\mathbf{Z_{s2}}$ are plotted in Fig. 11. It can be seen that $\angle Z_{qq}$ at magnitude interaction point 32 Hz is higher than -90^o, and phase angle difference is thus smaller than 180^o, which indicates that the system is stable. Corresponding time-domain simulation results are shown in Fig. 13, which agrees with the impedance-based stability analysis results. It can be seen from Figs. 11, 12 and 13 that the system is stabilized by optimizing the distribution of active and reactive power based on the proposed optimization method in this paper.

Compared with scheme 2, only active power dispatch is optimized in scheme 3, and only reactive power dispatch is optimized in scheme 4. The Bode diagrams of the total dq impedance matrices of the five paralleled GCIs in the two

TABLE II
CONTROLLER PARAMETERS OF POWER CONTROL LOOPS OF THE FIVE GCIS IN FIG. 1

Parameter	GCI 1	GCI 2	GCI 3	GCI 4	GCI 5
k_{pPQ}	2.7454e-5	3.0504e-5	3.4318e-5	4.2237e-5	5.4908e-5
k_{iPQ}	0.01648	0.01831	0.0206	0.02535	0.03295

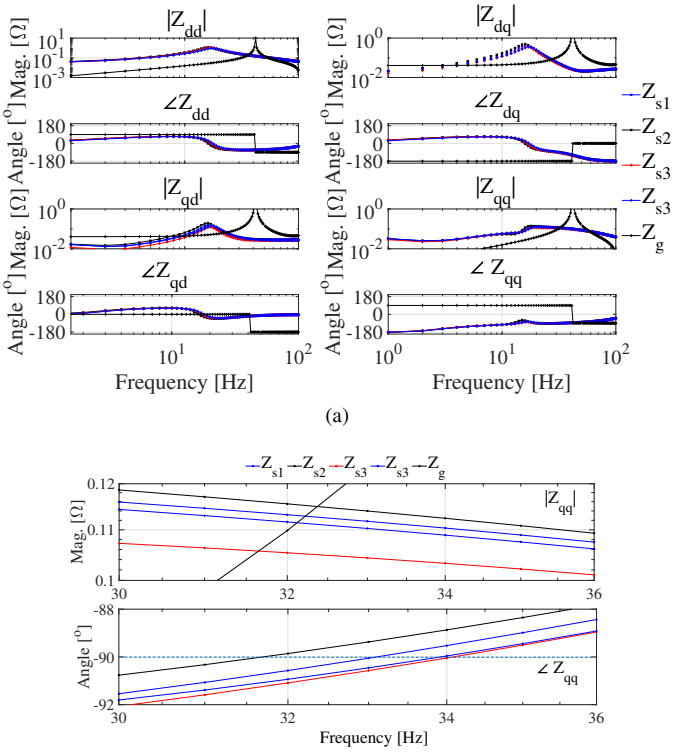

Fig. 11. Impedance-based stability analysis of the four schemes. (a) Bode diagrams of $\mathbf{Z_{tot}}$ and $\mathbf{Z_g}$. (b) Zoomed Bode diagrams of Z_{qq} component.

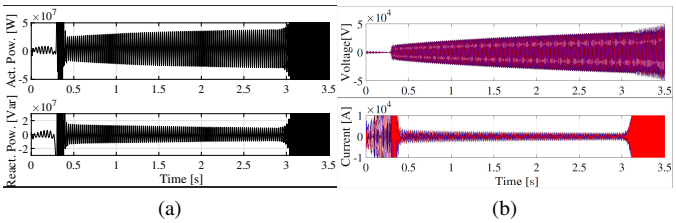

Fig. 12. Time-domain simulation results of scheme 1. (a) Simulation results of active and reactive power. (b) Simulation results of three-phase voltages and currents.

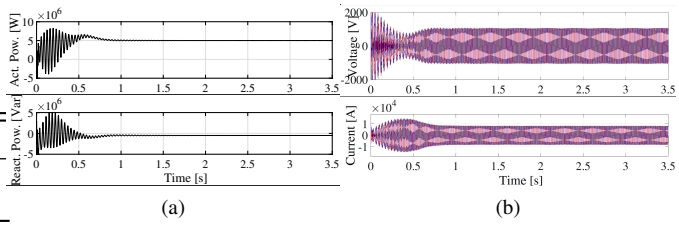

Fig. 13. Time-domain simulation results of scheme 2. (a) Simulation results of active and reactive power. (b) Simulation results of three-phase voltages and currents.

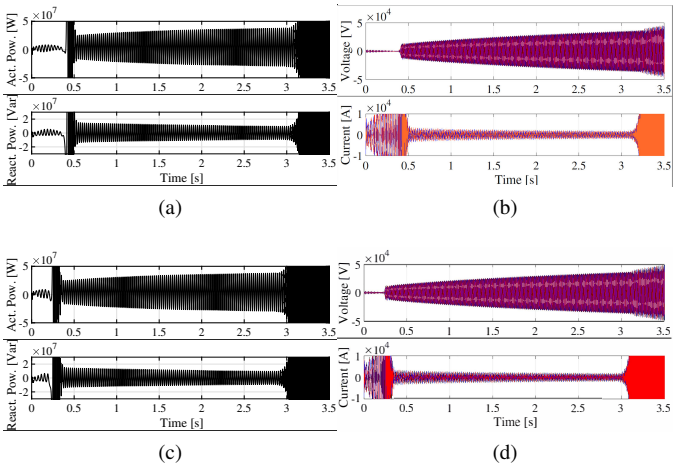

Fig. 14. Time-domain simulation results of scheme 3 and scheme 4. (a) Simulation results of active and reactive power of scheme 3. (b) Simulation results of three-phase voltages and currents of scheme 3. (c) Simulation results of active and reactive power of scheme 4. (d) Simulation results of three-phase voltages and currents of scheme 4.

schemes are shown as Z_{s3} and Z_{s4} in Fig. 11, respectively. It can be seen that $\angle Z_{qq}$ at magnitude interaction point 32 Hz is lower than -90^o, which indicates that the system is unstable under the two dispatch schemes. The corresponding time-domain simulation results of the two schemes are shown in Fig. 14. By comparing scheme 2 with schemes 3 and 4, it can be concluded that it's necessary to simultaneously optimize active power distribution and reactive power distribution to enhance system stability.

V. CONCLUSION

This paper investigates the impacts of active and reactive power on terminal impedance characteristics of GCI. On the basis of it, a novel active and reactive power dispatch method is proposed to enhance system stability in low-frequency range. According to the theoretical DQ impedance model of GCI, it's found that large active and reactive power references tend to violate and enhance passivity of GCI in low-frequency range, respectively. Furthermore, the maximum active power reference not to violate the passivity decreases, and the minimum reactive power reference to enforce the passivity increases if bandwidth of power control loop or PLL increases. The terminal impedance frequency responses of GCI obtained

TABLE III
FOUR SCHEMES OF ACTIVE AND REACTIVE POWER DISPATCH AMONG FIVE PARALLELED GCIS

Parameter	P_{ref1}	P_{ref2}	P_{ref3}	P_{ref4}	P_{ref5}	Q_{ref1}	Q_{ref2}	Q_{ref3}	Q_{ref4}	Q_{ref5}
Scheme 1	1 MW	1 MW	1 MW	1 MW	1 MW	0.5 MVar	0.5 MVar	0.5 MVar	0.5 MVar	0.5 MVar
Scheme 2	2 MW	1.5 MW	0.5 MW	0.5 MW	0.5 MW	0.25 MVar	0.25 MVar	0.25 MVar	0.75 MVar	1 MVar
Scheme 3	2 MW	1.5 MW	0.5 MW	0.5 MW	0.5 MW	1 MVar	0.75 MVar	0.25 MVar	0.25 MVar	0.25 MVar
Scheme 4	0.5 MW	0.5 MW	0.5 MW	1.5 MW	2 MW	0.25 MVar	0.25 MVar	0.25 MVar	0.75 MVar	1 MVar

Scheme 1: Without optimization. Scheme 2: With optimization of P_{tot} and Q_{tot}. Scheme 3: With only optimization of P_{tot}. Scheme 4: With only optimization of Q_{tot}.

by frequency sweeping validate the correctness of above theoretical analysis results. In addition, simulation results of a five-GCIs-based power system show that system stability can be enhanced, if active and reactive power are dispatched according to the proposed method. The proposed active and reactive power dispatch method is a supplement to the existing power dispatch algorithm neglecting stability violation in low-frequency range.

ACKNOWLEDGMENT

The authors wish to thank Dr. Raymundo E. Torres-Olguin from SINTEF Energy Research, Norway and Mr. Manuel Castillo from DigSILENT company, Germany for their valuable discussions and suggestions.

REFERENCES

[1] F. Blaabjerg, Z. Chen, and S. B. Kjaer, "Power electronics as efficient interface in dispersed power generation systems," *IEEE Trans. Power Electron.*, vol. 19, no. 5, pp. 1184–1194, Sep. 2004.

[2] J. L. Agorreta, M. Borrega, J. Lopez, and L. Marroyo, "Modeling and control of N-paralleled grid-connected inverters with LCL filter coupled due to grid impedance in PV plants," *IEEE Trans. Power Electron.*, vol. 26, no. 3, pp. 770–785, Mar. 2011.

[3] J. He, Y. W. Li, D. Bosnjak, and B. Harris, "Investigation and active damping of multiple resonances in a parallel-inverter-based microgrid," *IEEE Trans. Power Electron.*, vol. 28, no. 1, pp. 234–246, Jan. 2013.

[4] B. Wen, D. Boroyevich, R. Burgos, P. Mattavelli, and Z. Shen, "Analysis of DQ small-signal impedance of grid-tied inverters," *IEEE Trans. Power Electron.*, vol. 31, no. 1, pp. 675–687, Jan. 2016.

[5] W. Zhou, Y. Wang, and Z. Chen, "Frequency and temperature-dependent power cable modelling for small-signal stability analysis of grid-connected inverter system," in *Proc. 2018 IEEE Southern Power Electronics Conference (SPEC)*, Dec., pp. 1–8.

[6] Y. Wang, X. Wang, F. Blaabjerg, and Z. Chen, "Harmonic instability assessment using state-space modeling and participation analysis in inverter-fed power systems," *IEEE Trans. Ind. Electron.*, vol. 64, no. 1, pp. 806–816, Jan. 2017.

[7] W. Zhou, Y. Wang, and Z. Chen, "Impedance-based modelling method for length-scalable long transmission cable for stability analysis of grid-connected inverter," in *Proc. 2018 IEEE Southern Power Electronics Conference (SPEC)*, Dec., pp. 1–8.

[8] J. Sun, "Impedance-based stability criterion for grid-connected inverters," *IEEE Trans. Power Electron.*, vol. 26, no. 11, p. 3075, Nov. 2011.

[9] L. Xu and L. Fan, "Impedance-based resonance analysis in a VSC-HVDC system," *IEEE Trans. Power Del.*, vol. 28, no. 4, pp. 2209–2216, Oct. 2013.

[10] M. Amin, M. Molinas, J. Lyu, and X. Cai, "Impact of power flow direction on the stability of VSC-HVDC seen from the impedance Nyquist plot," *IEEE Trans. Power Electron.*, vol. 32, no. 10, pp. 8204–8217, Oct. 2017.

[11] D. Lu, X. Wang, and F. Blaabjerg, "Influence of reactive power flow on the DC-link voltage control in voltage-source converters," in *Proc. 2018 IEEE Energy Conversion Congress and Exposition (ECCE)*, Sep., pp. 2236–2241.

[12] D. Yang, X. Wang, and F. Blaabjerg, "Fast power control for VSCs to enhance the synchronization stability in ultra-weak grids," in *Proc. 2018 IEEE Power & Energy Society General Meeting (PESGM)*, pp. 1–6.

[13] T. Chen, C. K. Lee, and R. Hui, "A general design procedure for multi-parallel modular grid-tied inverters system to prevent common and interactive instability," *IEEE Trans. Power Electron.*, vol. 34, no. 7, pp. 6025–6030, Jul. 2019.

[14] C. Yoon, H. Bai, R. N. Beres, X. Wang, C. L. Bak, and F. Blaabjerg, "Harmonic stability assessment for multiparalleled, grid-connected inverters," *IEEE Trans. Sustain. Energy*, vol. 7, no. 4, pp. 1388–1397, Oct. 2016.

[15] H. Bai, X. Wang, and F. Blaabjerg, "Passivity enhancement in renewable energy source based power plant with paralleled grid-connected VSIs," *IEEE Trans. Ind. Appl.*, vol. 53, no. 4, pp. 3793–3802, Jul./Aug. 2017.

[16] M. Amin and M. Molinas, "A gray-box method for stability and controller parameter estimation in HVDC-connected wind farms based on nonparametric impedance," *IEEE Trans. Ind. Electron.*, vol. 66, no. 3, pp. 1872–1882, Mar. 2019.

[17] W. Zhou, Y. Wang, and Z. Chen, "A gray-box impedance reshaping method of grid-connected inverter for resonance damping," in *Proc. 2019 IEEE International Future Energy Electronics Conference and ECCE Asia (IFEEC 2019-ECCE Asia)*, pp. 1–8.

[18] D. Yang, X. Wang, F. Liu, K. Xin, Y. Liu, and F. Blaabjerg, "Adaptive reactive power control of PV power plants for improved power transfer capability under ultra-weak grid conditions," *IEEE Trans. Smart Grid*, vol. 10, no. 2, pp. 1269–1279, Mar. 2019.

[19] H. Zhao, Q. Wu, S. Huang, M. Shahidehpour, Q. Guo, and H. Sun, "Fatigue load sensitivity-based optimal active power dispatch for wind farms," *IEEE Trans. Sustain. Energy*, vol. 8, no. 3, pp. 1247–1259, Jul. 2017.

[20] H. Zhao, Q. Wu, J. Wang, Z. Liu, M. Shahidehpour, and Y. Xue, "Combined active and reactive power control of wind farms based on model predictive control," *IEEE Trans. Energy Convers.*, vol. 32, no. 3, pp. 1177–1187, Sep. 2017.